Numerical Simulation of the Atmospheric Signature of Artificial and Natural Seismic Events

Léo Martire, Quentin Brissaud, Voon Hui Lai, Raphaël F. Garcia, Roland Martin, Siddharth Krishnamoorthy, Attila Komjathy, Alexandre Cadu, James A. Cutts, Jennifer M. Jackson, et al.

Geophysical Research Letters

RESEARCH LETTER
10.1029/2018GL080485

Numerical Simulation of the Atmospheric Signature of Artificial and Natural Seismic Events

Léo Martire[1], Quentin Brissaud[2], Voon Hui Lai[2], Raphaël F. Garcia[1], Roland Martin[3], Siddharth Krishnamoorthy[4], Attila Komjathy[4], Alexandre Cadu[1], James A. Cutts[4], Jennifer M. Jackson[2], David Mimoun[1], Michael T. Pauken[4], and Anthony Sournac[1]

[1] Institut Supérieur de l'Aéronautique et de l'Espace/SUPAERO, Toulouse University, Toulouse, France, [2] Seismological Laboratory, California Institute of Technology, Pasadena, CA, USA, [3] Géosciences Environnement Toulouse, Toulouse University, Toulouse, France, [4] Jet Propulsion Laboratory, California Institute of Technology, Pasadena, CA, USA

Abstract The mechanical coupling between solid planets and their atmospheres enables seismically induced acoustic waves to propagate in the atmosphere. We numerically simulate this coupled system for two application cases: active seismic experiments (ASEs) and passive seismic experiments. A recent ASE (Krishnamoorthy et al., 2018, https://doi.org/10.1002/2018GL077481) observed the infrasonic signals produced by a seismic hammer. To measure the sensitivity of observations to seismic parameters, we attempt to reproduce the results from this experiment at short range by considering a realistic unconsolidated subsurface and an idealized rock-solid subsurface. At long range, we investigate the influence of the source by using two focal mechanisms. We found surface waves generate an infrasonic plane head wave in the ASE case of the rock-solid material. For the passive seismic experiments, the amplitude of atmospheric infrasound generated by seismic surface waves is investigated in detail. Despite some limitations, the simulations suggest that balloon measurement of seismically induced infrasound might help to constrain ground properties.

Plain Language Summary During an earthquake, the ground shakes the air above. We performed simulations of some seismic events and of the propagation of their consequences in the atmosphere. We found that observing the displacement of the air close to a seismic event can give information about the properties of the soil. This perspective is particularly interesting for planetary investigation. For example, it is impossible to study Venus' interior with ground instruments because of the harsh conditions at its surface. Our work is one of the steps toward proving that the study of Venus' (or any other solid planet) internal structure may be possible with airborne instruments.

Key Points:
- Full-wave numerical simulations of the 2-D coupled ground/atmosphere system under different seismic events are conducted
- For active seismic experiments, simulated short-range/low-altitude balloon signals depend significantly on near-surface velocity structure
- Active seismic experiment data and synthetics present the same seismic infrasound arrivals at similar frequencies

Supporting Information:
- Supporting Information S1

Correspondence to:
L. Martire,
leo.martire@isae-supaero.fr

Citation:
Martire, L., Brissaud, Q., Lai, V. H., Garcia, R. F., Martin, R., Krishnamoorthy, S., et al. (2018). Numerical simulation of the atmospheric signature of artificial and natural seismic events. *Geophysical Research Letters*, *45*. https://doi.org/10.1029/2018GL080485

Received 1 JUN 2018
Accepted 29 OCT 2018
Accepted article online 1 NOV 2018

1. Introduction

Atmospheric infrasounds originate from various processes (Le Pichon et al., 2010, section 6.2) such as explosions (Donn & Shaw, 1967; Posey & Pierce, 1971; Reed, 1969), object launches/reentries (Cotten et al., 1971; Evers et al., 2018; Garcés et al., 2004; ReVelle, 1976; Yamamoto et al., 2011), or the mechanical coupling between the atmosphere and the solid planet (Garcia et al., 2013; Le Pichon & Cansi, 2003; Lognonné & Johnson, 2007; Lognonnè et al., 2016; Mutschlecner & Whitaker, 2005; Young & Greene, 1982). Each process generates an infrasonic signal with a specific signature in terms of waveform and arrival time (Campus & Christie, 2010) that could help to characterize sources and underground properties.

However, the detectability of infrasounds is highly dependent on its amplitude. Two main processes impact the vertical propagation of acoustic signals in planetary atmospheres. First, the classical infrasound absorption processes act as a low-pass filter (Bass et al., 1984). Second, the decrease of density with altitude leads to the amplification of particle motion by conservation of kinetic energy but reduces the overpressure of mechanical signals propagating upward. Yet several papers have already demonstrated the detectability of infrasound using airborne barometers (Banister & Hereford, 1980a, 1980b, 1982a, 1982b, 1991; Bowman & Lees, 2015; Lees & Bowman, 2017; Lamb et al., 2018; Young et al., 2018). Balloon-borne instruments are thus expected to detect seismically induced infrasound and have a number of advantages: They are less subject to ground noise sources (turbulences and wind noise), they are generally smaller and/or lighter than their ground coun-

terparts, and they can act as in situ probes to measure wind speed and temperature. However, balloons are moving with atmospheric flows, and event observation is dependent on their localization (one could observe many events or miss some).

Based on the airborne barometers capability to detect seismoacoustic signals, Stevenson et al. (2015) present a feasibility study of the investigation of Venus' interior structure with seismological techniques. At the surface, atmospheric conditions are too extreme to consider landing ground stations, mainly because of the surface temperature (≃735 K). Atmospheric balloons could be a way to study the planet's interior without needing to land instruments, which would have to be remarkably robust to heat and pressure. Additionally, mechanical coupling between ground and atmosphere on Venus is known to be higher than on Earth (Garcia et al., 2005; Lognonné et al., 2016) because of surface density being 50 times larger on Venus than on Earth. To demonstrate the feasibility of an alternative airborne approach, the Jet Propulsion Laboratory (JPL) and its partners developed an active seismic experiment (ASE) in the Nevada desert in June 2017 to probe seismically induced acoustic waves with balloon sensors (Krishnamoorthy et al., 2018). The research on ASEs is intended to help develop a technique usable for detecting natural earthquakes (i.e., passive seismic experiments, PSEs). An experimental program on PSE is being planned for quakes occurring in Oklahoma (USA).

To better understand seismoacoustic dynamics and measure the sensitivity of observations on subsurface seismic parameters and source mechanisms, we numerically investigate the infrasound generation in a realistic coupled atmosphere-solid medium. We start by describing the simulation tool. We present the considered sources (for ASEs and PSEs) and the internal and atmospheric models used. Simulated receivers' positions are detailed. We examine the results of the simulations, compare one with field data, and interpret and discuss the simulated signals. Finally, we examine the prospect of ground imaging and event detection by using atmospheric balloons, describe limitations of the simulations, and detail the next steps in our work.

2. Ground/Atmosphere Numerical Simulations

2.1. Governing Equations and Numerical Method

The simulation tool, SPECFEM-DG, extends the routinely used SPECFEM software that employs a spectral element method (Komatitsch & Tromp, 1999; Komatitsch & Vilotte, 1998; Tromp et al., 2008) to model seismic wave propagation. SPECFEM-DG includes the propagation of waves in the atmosphere and is described in detail in Brissaud et al. (2017).

The atmospheric part of the simulations is performed through the solution of the full Navier-Stokes system of equations (Brissaud et al., 2017). The coupling at the solid/fluid boundary Γ_{FS} is done in both directions through the application of the following relations:

$$\text{on } \Gamma_{FS}, \quad \begin{cases} \mathbf{v}^f \cdot \mathbf{n} = \mathbf{v}^s \cdot \mathbf{n}, \\ \Sigma^s = \Sigma^f, \end{cases} \tag{1}$$

where $\mathbf{v}$ represent velocities, Σ are stress tensors, and f and s superscripts, respectively, indicate that quantities are those of the fluid and solid parts (Brissaud et al., 2017). Outer boundary conditions are chosen periodic on left/right boundaries and absorbing on the bottom (solid) and top (fluid) boundaries.

The numerical method relies on weak formulations through a spectral element method, continuous for the elastic domain (Komatitsch & Tromp, 1999; Komatitsch & Vilotte, 1998; Tromp et al., 2008), and discontinuous for the fluid domain (Brissaud et al., 2017). Time integration is explicit (optimal five-step fourth-order Runge-Kutta scheme; Carpenter & Kennedy, 1994).

Important assumptions made for the Navier-Stokes part are (1) an hydrostatic initial state and (2) a stratified atmospheric model (Brissaud et al., 2017). That is, the considered atmosphere must verify hydrostatic balance relations, the parameters must not vary horizontally, and wind must be horizontal. We ensure that those are verified for our applications by analytically constraining the atmospheric model (Brissaud, 2017).

2.2. Seismic Sources

Two different seismic sources are considered. First, for the ASE, we consider a seismic hammer (Hampshire & O'Donnell, 2013). The impact is modeled by a downward vertical point force of total duration 0.05 s (Gaussian wavelet with dominant frequency $f_0 = 20$ Hz), at 1-m depth. This modeling only reproduces linear seismic waves and no shock in the atmosphere. For the PSE, we consider earthquakes, modeled as point sources and given moment tensors. Because the seismoacoustic sources on other planets are not well constrained, we

Table 1
Ground Models

Model name	Layer	Thickness (m)	v_p (m/s)	v_s (m/s)	ρ (kg/m^3)	Q_p	Q_s
ASE-soft	1	8	652	150	1,560	40	20
	2	20	650	286	1,560	50	25
	3	52	1,942	571	2,050	100	50
	4	76	1,942	571	2,050	200	100
	5	bedrock	3,058	1,464	2,300	200	100
ASE-hard	1	156	1,942	744	2,050	174	100
	2	bedrock	3,058	1,464	2,300	163	100
PSE	1	500	2,500	1,070	2,110	20	10
	2	3,100	4,600	2,590	2,460	40	20
	3	12,960	6,100	3,530	2,740	500	600
	4	14,580	6,500	3,710	2,830	2,750	2,850
	5	12,960	6,900	3,930	2,920	3,000	3,100
	6	bedrock	8,140	4,520	3,350	3,000	3,100

Note. The first and second sets are used for the ASE simulations, while the third one is used for the two PSE simulations. v_p and v_s are the *P* and *S* waves velocities. ρ is the density. Q_p and Q_s are the quality factors of *P* and *S* waves, respectively. ASE-soft: thickness, v_p, v_s, and ρ from geophone data (Krishnamoorthy et al., 2018); quality factors from literature (Abercrombie, 1997). ASE-hard: all from literature (Barrett & Froggatt, 1978; Boore & Joyner, 1997; Coussy, 1987). PSE: thickness, v_p, v_s, and ρ from the CRUST1.0 (Laske et al., 2013) model of Oklahoma; Q_p in layers 1–2 (sediments) from (Aki & Wu, 1988, Figure 7, p. 92) and $Q_p = 2Q_s$; Q_p in layers 3–6 (crust and mantle) from (Aki & Wu, 1988, Figure 8, p. 96) and $Q_s = Q_p + 100$ (Hauksson & Shearer, 2006).

study the impact of various choices of focal mechanisms by considering two focal mechanisms: one 45° dip, generating high vertical displacement, and one 0° dip, generating nearly no vertical displacement. Based on Oklahoma's seismic studies (Grandin et al., 2017; McNamara et al., 2015), we choose the event to occur at 5-km depth and a magnitude $M_w = 2.5M_0 \simeq 6.31 \times 10^{12}$N·m (Kanamori, 1977). Functional forms of the source functions are given in Texts S1 and S2 in the supporting information. Note that since the PSEs are modeled by 1-D faults in 2-D domains, their magnitudes are rescaled by the typical fault length (Westwood et al., 2017; Text S2).

2.3. Internal Structure Models

For the ASE, we set up two soil models: *ASE-soft*, inferred from geophone data of the JPL experiment (Krishnamoorthy et al., 2018) and composed of unconsolidated layers, and *ASE-hard*, composed only of hard rock whose parameters are deduced from expertise and literature (Barrett & Froggatt, 1978; Boore & Joyner, 1997; Coussy, 1987; e.g., silty claystone, volcanic breccia, or saturated shales/clays). We use ASE-hard to study the atmospheric signals' sensitivity to soil hardness. For both, bedrock is chosen to be identical, and the layers above amount to the same total thickness. For the PSE, we utilize a CRUST1.0 (Laske et al., 2013) model of Oklahoma down to 45-km depth. Table 1 summarizes all approaches.

2.4. Atmospheric Models

Two atmospheric models are chosen for this investigation. For the ASE, we use a windless isothermal atmospheric model (at short range and low altitudes, wind appears not to play a significant role). The parameters are defined as (SI units) follows: $\rho(z) = \rho_0 e^{-\frac{z}{H}} = 1.4e^{-\frac{z}{10^4}}$, $g_z = 9.81$, $p(z) = \rho(z)g(z)H$ (hydrostatic hypothesis), $\gamma = 1.401$, $\mu = 1 \times 10^{-8}$, and no thermal conductivity ($\kappa = 0$). For the PSE, which is a long-range simulation, we extracted from MSISE00 (Hedin, 1991) and HWM93 (Hedin et al., 1996) an atmospheric model for Oklahoma taking wind into account (Figure S6). For all models, we make sure the two Navier-Stokes hypotheses (see section 2.1) hold.

2.5. Simulation Domains and Receivers

For the ASE, the computational domain is $4,000 \times 908$ m, including 600 m of atmosphere. For the PSE, it is 300×83 km, 35 km of atmosphere. Simulated sensors' positions are chosen according to possible positions of real sensors. In both simulations, ground arrays monitor vertical velocity and pressure perturbation. In the ASE, vertical arrays of microbarometers are added: a low-altitude one (tethered balloons) and a high-altitude one

(hot-air balloons; Krishnamoorthy et al., 2018). In the PSE, horizontal arrays of barometers located at altitudes of 15 and 30 km are added (tropo/stratospheric balloons).

2.6. Benchmark With FK Method

To validate the code, we compare the ASE synthetics obtained with SPECFEM2D-DG with those generated using a 1-D frequency-wavenumber (FK) code, which uses the Thompson-Haskell propagator matrix to calculate the elastodynamic solutions for point sources in a multilayered half-space (Zhu & Rivera, 2002). Figures S3 and S4 show that the synthetics obtained with the two methods compare well: Arrival times, waveforms, phases, and frequency contents agree practically exactly.

3. Results

3.1. ASE Short-Range Propagation

3.1.1. Results From Short-Range Simulations

In the near surface, because of very low shear wave velocities, the surface wave (SW) velocity v_s is less than c, the speed of sound in air, for ASE-soft (respectively $v_s > c$ for ASE-hard). Because of this difference in ground structure, seismic SWs will propagate slower (respectively faster) than any atmospheric signal.

For the two ASE simulations, synthetics were recorded at a vertical array of stationary airborne barometers located 300 m away from impact.

As shown in Figure 1, for both models, the ground drop due to the impact generates an atmospheric quasi-spherical wave (SpW). Moreover, for both models, *P*-diffracted waves (*P* waves traveling through bedrock and back up) generate low-amplitude plane infrasound induced by *P*-diffracted waves (PDI). For ASE-soft, strong ground oscillations due to *P* waves reflections in the layered soil generate epicentral infrasound (EI), which is not the case for ASE-hard, since the ground is less layered and/or resonant. For ASE-hard, the seismic SWs due to the impact generate ground motions ahead of the spherical wave and thus a high-amplitude plane head infrasound (HI). In ASE-soft, EI's amplitude decreases with altitude. In ASE-hard, amplitude of the HI is almost constant with altitude (Figure S10).

3.1.2. Comparison: SPECFEM-DG Synthetics and Experimental Shots

A comparison between our ASE-soft synthetics and hammer shots' data from the JPL experiment (Krishnamoorthy et al., 2018) is presented in Figure 2.

The initial high-amplitude shock wave of the hammer against the metal plate is visible in the data but not in the synthetics: Our source modeling does not capture this effect. We observe the concordance of *P*/*S* waves arrival times in the v_z time series. Additionally, in all time series, the timing of phases and root-mean-square amplitude with time show broad agreement; however, the phase and frequency content are not matched. For airborne signals, both in synthetics and data, we also remark that the EI amplitude decreases with altitude. Because of the idealized simulated soil, attenuation and thus dispersion can significantly differ from the real case. Moreover, lateral variations of the first layer thickness cannot be considered negligible over the $\simeq$170 m of propagation. It is thus reasonable not to expect the exact same frequency content at such high frequencies (>5 Hz), and consequently, agreement quantification by waveform misfit is not appropriate. Furthermore, ground synthetics contain more low frequencies than ground data; consequently, the synthetic EI has also lower frequency than the observed infrasound. These results are encouraging because they show that the physical processes are sufficiently well reproduced, and we now aim at improving the subsurface modeling.

3.1.3. Two-Dimensional to 3-D Geometrical Spreading Rescaling

Two-dimensional synthetics can simply be rescaled by a factor $r^{-1/2}$ in order to take geometric spreading into account.

Axisymmetric simulations enabling 3-D-like propagation were performed using the classical SPECFEM software in order to support this argument (Figure S9). Note, however, that those simulations cannot take wind or viscosity into account nor model point moment sources.

Yet, if the paths followed by those waves are intricate, a simple rescaling could fail in modeling geometrical spreading. More generally, 3-D simulations would be needed in order to extend our conclusions to a broader

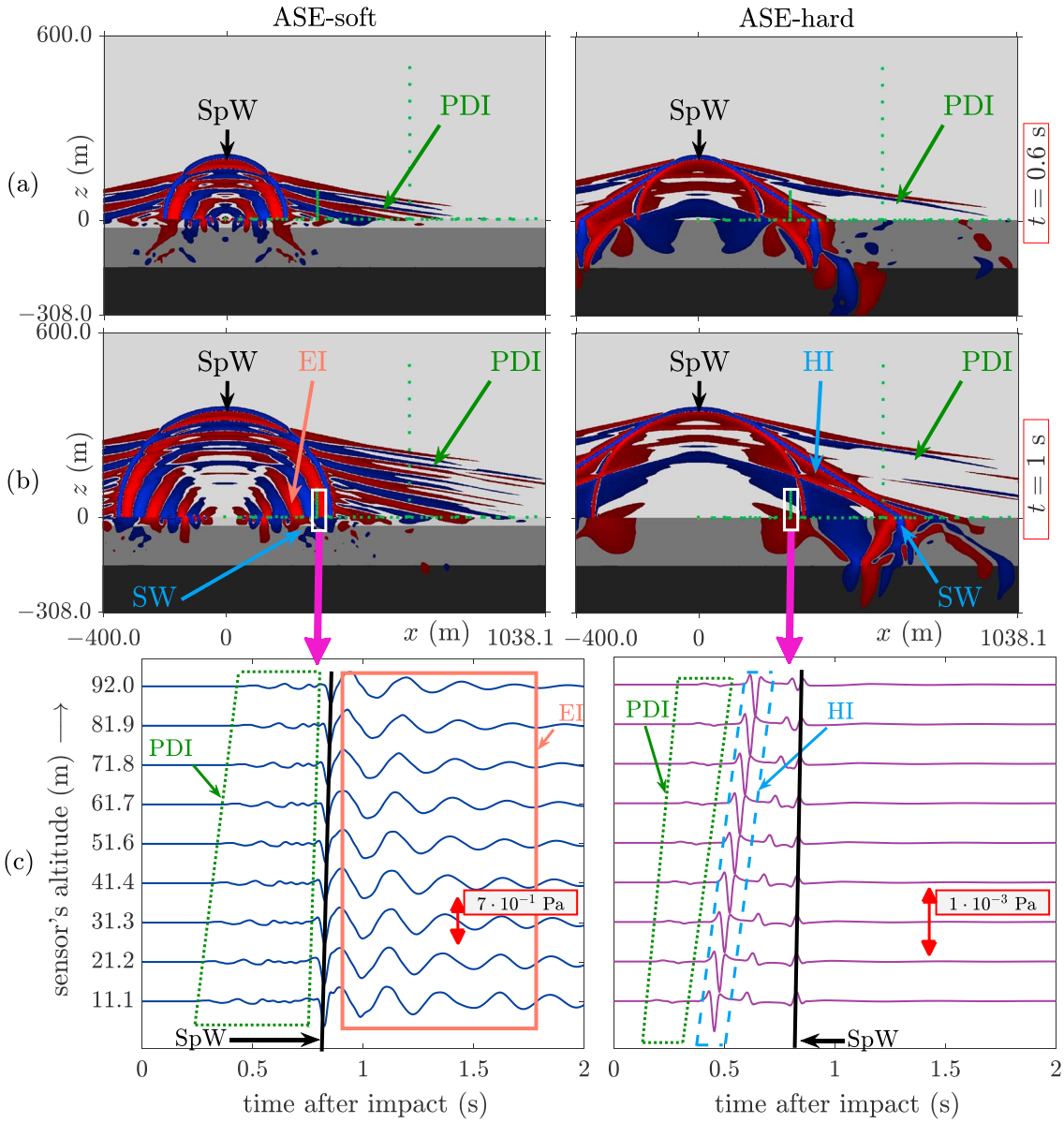

Figure 1. (a and b) Snapshots (pressure perturbations in the atmosphere, vertical velocity on the ground, red for values > 1% of maximum amplitude, blue for < −1%) of the active seismic experiment (seismic hammer) simulations, at (a) $t = 0.6$ s and (b) $t = 1$ s. (c) Pressure perturbation synthetics for the active seismic experiment (seismic hammer) simulations, as function of time, for a vertical array of stations 300 m away from the source (highlighted by the white square in the snapshots). (left column) Soft soil and (right column) hard soil. Labels: SpW = spherical wave; EI = epicenter infrasound; SW = surface waves; PDI = *P*-diffracted waves infrasound; HI = head infrasound.

context. They are computationally more expensive but will be done in the future, using the 3-D version of SPECFEM-DG.

3.2. PSE Long-Range Propagation

For the two PSE simulations, synthetics were recorded at a 15-km altitude horizontal array of stationary airborne barometers.

As shown in Figure S7, the 0° dip earthquake (PSE-0) does not radiate much energy right above the source, to the contrary of the 45° dip one (PSE-45). As presented on Figure 3, the atmospheric infrasound away from the source is dominantly generated by seismic SWs. Consequently, just as SWs, its amplitude decreases with horizontal distance. For SWs, the decreasing amplitude is due both to intrinsic and geometric attenuation (Figure S7).

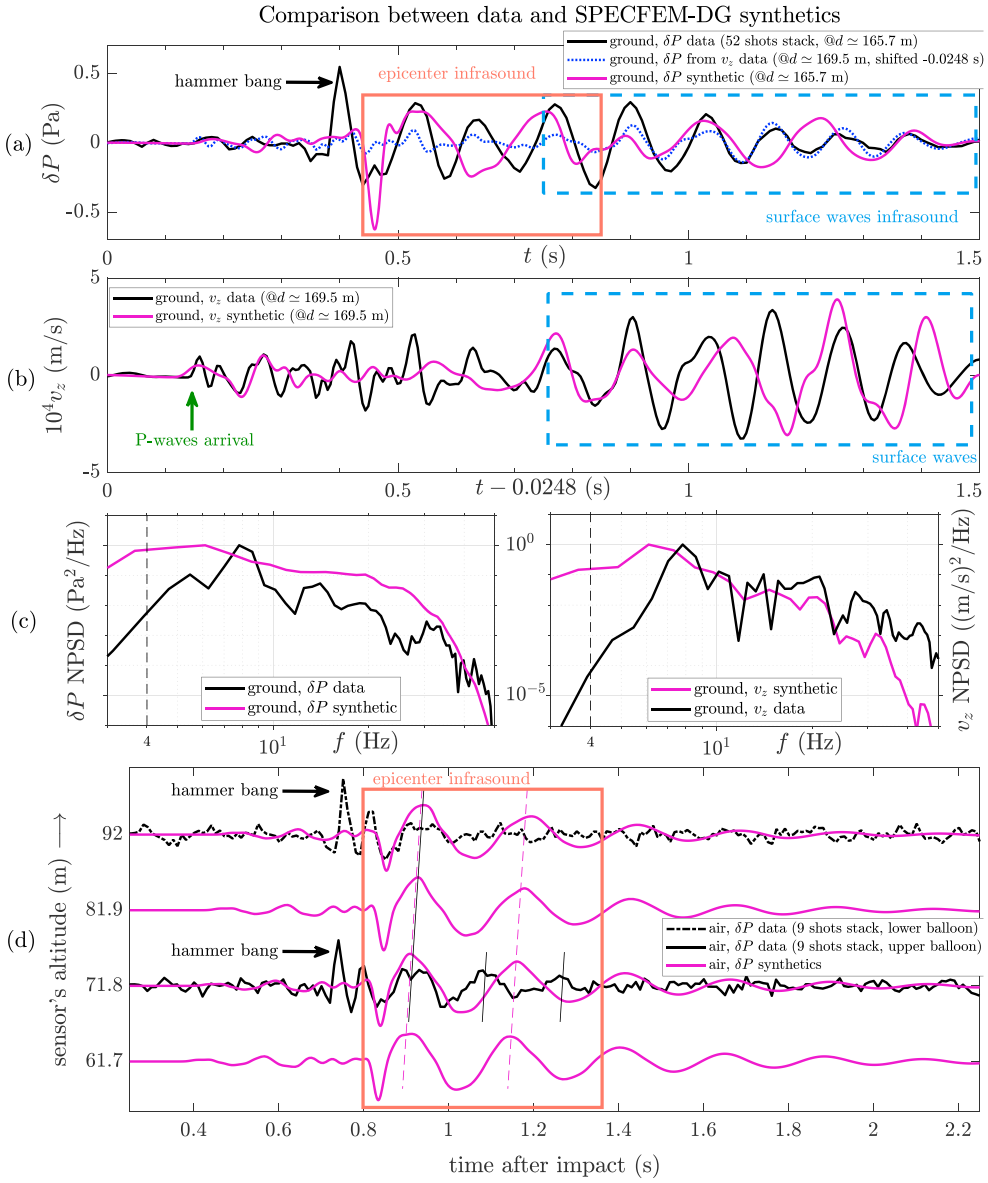

Figure 2. Comparison bewteen data and SPECFEM-DG active seismic experiment on soft soil synthetics. (a) Ground pressure perturbation, (b) ground vertical velocity, (c) normalized power spectral densities (NPSDs; left for ground pressure perturbation [a] and right for ground vertical velocity [b]), and (d) airborne pressure perturbation. All recordings and synthetics were filtered using a high-pass Butterworth filter with a 4-Hz cutoff frequency. δP in (a) is recorded on ground and ≃165 m away from impact; v_z in (b) is recorded on ground and ≃169 m away from impact. Since the seismometer is ≃ 3.7248 m further away from the hammer than the barometer, signals in (b) were shifted by $3.7248/v_s = 3.7248/150 \simeq 0.0248$ s to ease comprehension. The *δP from v_z* plot in (a) is obtained by converting v_z data (see [b]) to pressure perturbation through impedance. The barometer stack in (a) was time shifted to match the δP from v_z signal. The barometer stacks in (d) were time shifted to match the corresponding first epicentral infrasound in the synthetics. Slim diagonal lines in (d) highlight the epicentral infrasound overpressure bumps both in data and synthetics. Note that the high-frequency downward peak in the barometer synthetics (at $t \simeq 0.45$ s in [a] and at $t \simeq 0.85$ s in [d]) cannot be due to the hammer hitting the metal plate, as we do not model it.

4. Discussion and Conclusion

SWs propagate at approximately the *S* wave velocity v_s (Freund, 1997, equation (2.5.13)). For ASE-hard, since $v_s \gg c$ the air sound velocity, the SWs cause a rapid ground motion and thus a pressure perturbation in the air, which over a distance will generate plane waves in the atmosphere. This phenomenon is the cause of the high-amplitude head infrasound (HI) observed in the ASE-hard simulations (HI). For ASE-soft, SW velocity

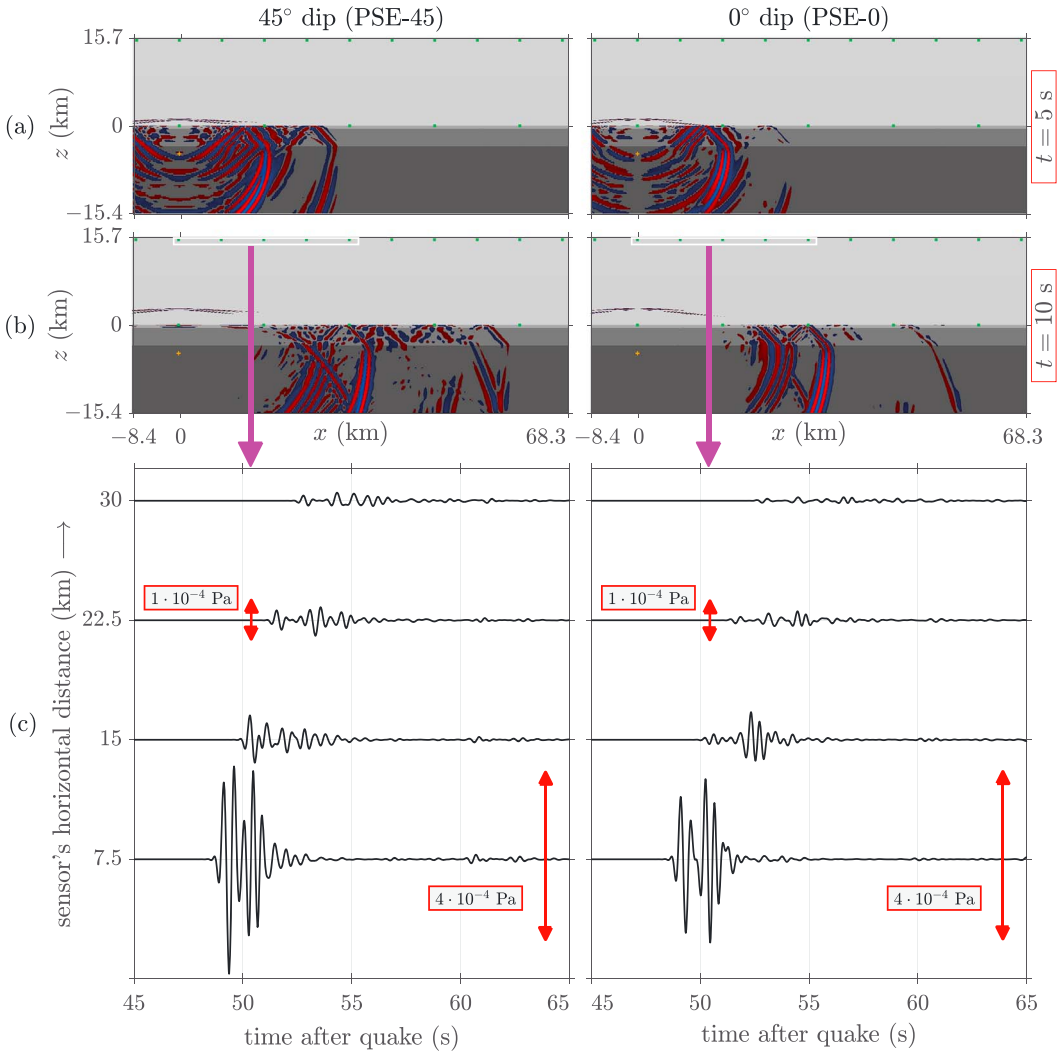

Figure 3. (a and b) Snapshots (pressure perturbations in the atmosphere, vertical velocity on the ground, red for values > 1% of maximum amplitude, blue for < −1%) of the passive seismic experiment (earthquakes) simulations, at (a) $t = 5$ s and (b) $t = 10$ s. (c) Pressure perturbation synthetics for the passive seismic experiment (earthquakes) simulations, as function of time, for an horizontal array of stations at altitude 15 km. (left column) 45° dip and (right column) 0° dip. The synthetics were not filtered. The decrease of amplitude with horizontal distance appears clearly, and is due to the decrease in amplitude of the generating surface waves (Figure S7).

$v_s < c$; hence, high-amplitude HI is not produced, and only signals due to *P* diffracted waves are visible (*P*-diffracted waves infrasound). The low amplitude of the latter is expected to make them more difficult to detect than the high-amplitude infrasound created by SWs on hard soil.

Moreover, during the JPL experiment (Krishnamoorthy et al., 2018), ground sensors deployed in the impact zone were clipped. In ASE-soft, airborne sensors monitored the infrasound created by ground movements close to the source (EI), potentially making them a viable alternative to clipped ground sensors. This prospect is currently being investigated in rigorous detail.

We remarked that, on hard soil ($v_s \gg c$), the amplitude of the HIs generated by the seismic SWs barely decreases with altitude and furthermore that this phenomenon appears both in 2-D and 3-D (Figure S10). This type of propagation, being fully vertical, has a low sensitivity to horizontal winds. The amplitude of this HIs only depends on the amplitude of the generating SWs, and this whatever the altitude. Finally, viscoelastic attenuation also plays a role, which is far from negligible at large distances; however, its effect will be most important only for high-frequency phenomena. Figures S8–S10 illustrate all those arguments. The decrease in density might mitigate this conclusion when considering higher altitudes.

In the PSE simulations, directly above the source, the amplitudes of infrasound significantly depend on the source mechanism. However, for a given horizontal distance away from the epicenter, they are comparable, since seismic SWs generate them. Yet, in general, the dependency of SWs' amplitudes on source mechanism and depth of the event (Tsai & Aki, 1971, Figures 6 and 7; Aki & Richards, 2002, section 7.5) has to be taken into account. Finally, this amplitude quickly decreases with distance because of geometric ($\propto r^{-1/2}$) and intrinsic attenuations (Figure 3).

Note that, the waves remaining linear, the presented PSE amplitudes can be rescaled up for higher-magnitude quakes (Text S2).

Barometers integrated on balloon platforms could thus record signals coming from ground events and therefore help to constrain subsurface models. Indeed, SW-induced infrasound can retain characteristics of seismic movements.

More simulations are planned to define more precisely which geometrical and physical cases can be studied and/or that related balloon configurations could be used. In particular, 3-D simulations including topography (mountain ranges, etc.), different types of sources (other earthquake source mechanisms, atmospheric explosions, microbaroms, etc.), and/or more accurate ground models will be performed. Those studies will be other opportunities to investigate further atmospheric propagation effects, which were not completely addressed here for brevity.

Acknowledgments
The authors thank the CALMIP computing center (Toulouse, France) for computer resources (project p1404). The authors thank both the "Direction Générale de l'Armement" (French DoD) and the "Région Occitanie" for funding the PhD grant of Léo Martire. This study was supported by CNES research projects and the W. M. Keck Institute for Space Studies. Contributions from JPL authors were made possible by research carried out with support from an internal research and technology grant at the Jet Propulsion Laboratory, California Institute of Technology, under a contract with the National Aeronautics and Space Administration. Data used to generate results presented here have been uploaded to publicly accessible repositories: https://doi.org/10.5281/zenodo.1421100 for the seismometer data and https://doi.org/10.6084/m9.figshare.6137507 for the barometer data.

References

Abercrombie, R. E. (1997). Near-surface attenuation and site effects from comparison of surface and deep borehole recordings. *Bulletin of the Seismological Society of America*, *87*(3), 731–744.

Aki, K., & Richards, P. G. (2002). *Quantitative seismology* (2nd ed.). Sausalito, CA: University Science Books.

Aki, K., & Wu, R.-S. (1988). *Scattering and attenuations of seismic waves*. Basel: Springer Basel. https://doi.org/10.1007/978-3-0348-7722-0

Banister, J. R., & Hereford, W. V. (1980a). Preliminary report on hearts high altitude pressure measurements (Tech. rep.). Albuquerque, NM: Sandia National Laboratories.

Banister, J. R., & Hereford, W. V. (1980b). Farm high altitude pressure measurements and analysis (Tech. rep.). Albuquerque, NM: Sandia National Laboratories.

Banister, J. R., & Hereford, W. V. (1982a). Rummy high-altitude pressure measurements and analysis (Tech. rep.). Albuquerque, NM: Sandia National Laboratories.

Banister, J. R., & Hereford, W. V. (1982b). Jornada high altitude pressure measurements (Tech. rep.). Albuquerque, NM: Sandia National Laboratories.

Banister, J. R., & Hereford, W. V. (1991). Observed high-altitude pressure waves from an underground and a surface explosion. *Journal of Geophysical Research*, *96*(90), 5185–5193.

Barrett, P. J., & Froggatt, P. C. (1978). Densities, porosities, and seismic velocities of some rocks from Victoria Land, Antarctica. *New Zealand Journal of Geology and Geophysics*, *21*(2), 175–187. https://doi.org/10.1080/00288306.1978.10424049

Bass, H. E., Sutherland, L., Piercy, J., & Evans, L. (1984). Absorption of sound by the atmosphere. In W. P. Mason (Ed.), *Physical acoustics: Principles and methods (A85-28596 12-71)* (Vol. 17, pp. 145–232). Orlando, FL: Academic Press, Inc.

Boore, D. M., & Joyner, W. B. (1997). Site amplifications for generic rock sites. *Bulletin of the Seismological Society of America*, *87*(2), 327–341.

Bowman, D. C., & Lees, J. M. (2015). Infrasound in the middle stratosphere measured with a free-flying acoustic array. *Geophysical Research Letters*, *42*, 10,010–10,017. https://doi.org/10.1002/2015GL066570

Brissaud, Q. (2017). Modélisation numérique des ondes atmosphériques issues des couplages solide/océan/atmosphère et applications (Ph.D. thesis), Université Toulouse 3 Paul Sabatier.

Brissaud, Q., Martin, R., Garcia, R. F., & Komatitsch, D. (2017). Hybrid Galerkin numerical modelling of elastodynamics and compressible Navier-Stokes couplings: Applications to seismo-gravito acoustic waves. *Geophysical Journal International*, *210*(2), 1047–1069. https://doi.org/10.1093/gji/ggx185

Campus, P., & Christie, D. R. (2010). Worldwide observations of infrasonic waves. In A. Le Pichon, E. Blanc, & A. Hauchecorne (Eds.), *Infrasound monitoring for atmospheric studies* (pp. 185–234). Dordrecht: Springer.

Carpenter, M. H., & Kennedy, C. A. (1994). Fourth-order 2N-storage Runge-Kutta schemes. *Nasa Technical Memorandum*, *109112*, 1–26.

Cotten, D. E., Donn, W. L., & Oppenheim, A. (1971). On the generation and propagation of shock waves from Apollo rockets at orbital altitudes. *Geophysical Journal of the Royal Astronomical Society*, *26*(1-4), 149–159. https://doi.org/10.1111/j.1365-246X.1971.tb03388.x

Coussy, O. (1987). Acoustics of porous media, Editions Technip.

Donn, W. L., & Shaw, D. M. (1967). *Reviews of Geophysics*, *5*, 53–82. https://doi.org/10.1029/RG005i001p00053

Evers, L. G., Assink, J. D., Smets, P. S. M., & Miller, S. (2018). Infrasound from the 2009 and 2017 DPRK rocket launches. *Geophysical Journal International*, *213*(April), 1785–1791. https://doi.org/10.1093/gji/ggy092/4925577

Freund, J. B. (1997). Proposed inflow/outflow boundary condition for direct computation of aerodynamic sound. *AIAA Journal*, *35*(4), 740–742. https://doi.org/10.2514/2.167

Garcés, M. M., Bass, H. E., Drob, D. P., Hetzer, C., Hedlin, M., Le Pichon, A., et al. (2004). Forensic studies of infrasound from massive hypersonic sources. *Eos*, *85*(43), 433. https://doi.org/10.1029/2004EO430002

Garcia, R. F., Bruinsma, S., Lognonné, P., Doornbos, E., & Cachoux, F. (2013). GOCE: The first seismometer in orbit around the Earth. *Geophysical Research Letters*, *40*, 1015–1020. https://doi.org/10.1002/grl.50205

Garcia, R. F., Lognonné, P., & Bonnin, X. (2005). Detecting atmospheric perturbations produced by Venus quakes. *Geophysical Research Letters*, *32*, L16205. https://doi.org/10.1029/2005GL023558

Grandin, R., Vallée, M., & Lacassin, R. (2017). Rupture process of the *Mw* = 5.8 Pawnee, Oklahoma, earthquake from Sentinel 1 InSAR and seismological data. *Seismological Research Letters*, *88*(4), 994–1004. https://doi.org/10.1785/0220160226

Hampshire, J. B., & O'Donnell, J. (2013). The seismic hammer. In *Seismic Instrumentation Technology Symposium, Incorporated Research Institutions for Seismology, Albuquerque, New Mexico, USA*.
Hauksson, E., & Shearer, P. M. (2006). Attenuation models (Qp and Qs) in three dimensions of the southern California crust: Inferred fluid saturation at seismogenic depths. *Journal of Geophysical Research*, *111*, B05302. https://doi.org/10.1029/2005JB003947
Hedin, A. E. (1991). Extension of the MSIS thermosphere model into the middle and lower atmosphere. *Journal of Geophysical Research*, *96*(A2), 1159–1172. https://doi.org/10.1029/90JA02125
Hedin, A. E., Fleming, E. L., Manson, A. H., Schmidlin, F. J., Avery, S. K., Clark, R. R., et al. (1996). Empirical wind model for the upper, middle and lower atmosphere. *Journal of Atmospheric and Terrestrial Physics*, *58*(13), 1421–1447. https://doi.org/10.1016/0021-9169(95)00122-0
Kanamori, H. (1977). The energy release in great earthquakes. *Journal of Geophysical Research*, *82*(20), 2981–2987. https://doi.org/10.1029/JB082i020p02981
Komatitsch, D., & Tromp, J. (1999). Introduction to the spectral element method for three-dimensional seismic wave propagation. *Geophysical Journal International*, *139*, 806–822.
Komatitsch, D., & Vilotte, J.-P. (1998). The spectral element method: An efficient tool to simulate the seismic response of 2D and 3D geological structures. *Bulletin of the Seismological Society of America*, *88*(2), 368–392. https://doi.org/10.1.1.716.9673
Krishnamoorthy, S., Komjathy, A., Pauken, M. T., Cutts, J. A., Garcia, R. F., Mimoun, D., et al. (2018). *Detection of artificially generated seismic signals using balloon-borne infrasound sensors* (Vol. 45, pp. 3393–3403). https://doi.org/10.1002/2018GL077481
Lamb, O. D., Lees, J. M., & Bowman, D. C. (2018). Detecting lightning infrasound using a high-altitude balloon. *Geophysical Research Letters*, *45*, 7176–7183. https://doi.org/10.1029/2018GL078401
Laske, G., Masters, G., Ma, Z., & Pasyanos, M. E. (2013). Update on CRUST1. 0 - A 1-degree global model of Earth's crust, Geophys. Res. Abstract, 15, Abstract EGU2013–2658.
Le Pichon, A., Blanc, E., & Hauchecorne, A. (2010). *Infrasound monitoring for atmospheric studies*. Dordrecht, Netherlands: Springer. https://doi.org/10.1007/978
Le Pichon, A., & Cansi, Y. (2003). PMCC for infrasound data processing. *Handbook of Signal Processing in Acoustics*, *2*(2), 1–9.
Lees, J. M., & Bowman, D. C. (2017). Balloon borne infrasound platforms: Low noise, high yield. *The Journal of the Acoustical Society of America*, *141*(5), 4046–4046. https://doi.org/10.1121/1.4989354
Lognonné, P., Karakostas, F., Rolland, L., & Nishikawa, Y. (2016). Modeling of atmospheric-coupled Rayleigh waves on planets with atmosphere: From Earth observation to Mars and Venus perspectives. *The Journal of the Acoustical Society of America*, *140*(2), 1447–1468. https://doi.org/10.1121/1.4960788
Lognonné, P., & Johnson, C. (2007). Planetary Seismology 64 pp., Institut de Physique du Globe de Paris.
McNamara, D. E., Benz, H. M., Herrmann, R. B., Bergman, E. A., Earle, P., Holland, A., et al. (2015). Earthquake hypocenters and focal mechanisms in central Oklahoma reveal a complex system of reactivated subsurface strike-slip faulting. *Geophysical Research Letters*, *42*, 2742–2749. https://doi.org/10.1002/2014GL062730
Mutschlecner, J. P., & Whitaker, R. W. (2005). Infrasound from earthquakes. *Journal of Geophysical Research*, *110*, D01108. https://doi.org/10.1029/2004JD005067
Posey, J. W., & Pierce, A. D. (1971). Estimation of nuclear explosion energies from microbarograph records. *Nature*, *232*, 253. https://doi.org/10.1038/232253a0
ReVelle, D. O. (1976). On meteor-generated infrasound. *Journal of Geophysical Research*, *81*(7), 1217–1230. https://doi.org/10.1029/JA081i007p01217
Reed, J. W. (1969). Climatology of airblast propagations from Nevada test site nuclear airbursts (Tech. Rep. SC-RR-69-572). New Mexico, USA: Sandia National Laboratories Albuquerque.
Stevenson, D., Cutts, J., & Mimoun, D. (2015). Probing the interior structure of Venus (Tech. rep.). Pasadena, CA: Keck Institute for Space Studies.
Tromp, J., Komatitsch, D., & Liu, Q. (2008). *Spectral-element and adjoint methods in seismology*, vol. 3, pp. 1–32.
Tsai, Y.-B., & Aki, K. (1971). Amplitude spectra of surface waves from small earthquakes and underground nuclear explosions. *Journal of Geophysical Research*, *76*(17), 3940–3952. https://doi.org/10.1029/JB076i017p03940
Westwood, R. F., Toon, S. M., Styles, P., & Cassidy, N. J. (2017). Horizontal respect distance for hydraulic fracturing in the vicinity of existing faults in deep geological reservoirs: A review and modelling study. *Geomechanics and Geophysics for Geo-Energy and Geo-Resources*, *3*(4), 379–391. https://doi.org/10.1007/s40948-017-0065-3
Yamamoto, M. Y., Ishihara, Y., Hiramatsu, Y., Kitamura, K., Ueda, M., Shiba, Y., et al. (2011). Detection of acoustic/infrasonic/seismic waves generated by hypersonic re-entry of the HAYABUSA capsule and fragmented parts of the spacecraft. *Publications of the Astronomical Society of Japan*, *63*(5), 971–978. https://doi.org/10.1093/pasj/63.5.971
Young, E. F., Bowman, D. C., Lees, J. M., Klein, V., Arrowsmith, S. J., & Ballard, C. (2018). Explosion-generated infrasound recorded on ground and airborne microbarometers at regional distances. *Seismological Research Letters*, *89*(4), 1497–1506. https://doi.org/10.1785/0220180038
Young, J. M., & Greene, G. E. (1982). Anomalous infrasound generated by the Alaskan earthquake of 28 March 1964. *Journal of the Acoustical Society of America*, *71*(2), 334–339. https://doi.org/10.1121/1.387457
Zhu, L., & Rivera, L. A. (2002). Computation of dynamic and static displacement from a point source in multi-layered media. *Geophysical Journal International*, *148*(August), 619–627.